metals

MDPI

Article

Energy Density Effect of Laser Alloyed TiB_2/TiC/Al Composite Coatings on LMZ/HAZ, Mechanical and Corrosion Properties

Dunja Ravnikar [1], Uroš Trdan [1,*], Aleš Nagode [2] and Roman Šturm [1]

[1] Faculty of Mechanical Engineering, University of Ljubljana, Aškerčeva 6, 1000 Ljubljana, Slovenia; dunja.ravnikar@fs.uni-lj.si (D.R.); roman.sturm@fs.uni-lj.si (R.Š.)

[2] Faculty of Natural Sciences and Engeneering, University of Ljubljana, Aškerčeva 12, 1000 Ljubljana, Slovenia; ales.nagode@omm.ntf.uni-lj.si

* Correspondence: uros.trdan@fs.uni-lj.si; Tel.: +386-1-477-1432

Received: 17 February 2020; Accepted: 18 March 2020; Published: 23 March 2020

Abstract: In the present work, TiC/TiB_2/Al composite coatings were synthesized onto a precipitation hardened AlSi1MgMn alloy by laser surface alloying (LSA), using 13.3 J/mm^2 and 20 J/mm^2 laser energy densities. Microstructure evaluation, microhardness, wear and corrosion performance were investigated and compared with the untreated/substrate Al alloy sample. The results confirmed sound, compact, crackles composite coating of low porosity, with a proper surface/substrate interface. Microstructural analyses revealed the formation of extremely fine nano-precipitates, ranging from of 50–250 nm in the laser melted (LMZ) and large precipitates, accompanied with grain coarsening in the heat-affected zone (HAZ), due to the substrate overheating during the LSA process. Nonetheless, both coatings achieved higher microhardness, with almost 7-times higher wear resistance than the untreated sample as a consequence of high fraction volume of hard, wear resistant TiB_2 and TiC phases inside the composite coatings. Further, cyclic polarization results in 0.5 M NaCl aqueous solution confirmed general improvement of corrosion resistance after LSA processed samples, with reduced corrosion current by more than a factor of 9, enhanced passivation/repassivation ability and complete prohibition of crystallographic pitting, which was detected with the untreated Al alloy.

Keywords: laser surface alloying (LSA); ceramic coatings on Al alloy; microstructure; laser melted/heat affected zone (LMZ/HAZ); microhardness; wear; corrosion

1. Introduction

Aluminium alloys are used extensively in automobile and aerospace applications mainly due to good strength-to-weight ratio, ductility, lightweight, availability and low cost [1–4]. These alloys are also inherently resistant to corrosion and oxidation due to spontaneous formation of thin surface passive films [3,5]. However, this thin oxide film (2–9 nm) does not provide sufficient resistance to corrosion even in weakly corroding media [6]. The presence of Cl^-, F^-, I^- and Br^- ions in the solution increases the sensitivity of Al alloys towards localized corrosion [3]. Furthermore, low hardness and poor tribological properties of Al alloys represent a critical factor when wear is involved [1,2,4]. Hence, additional protection to enhance resistance to localized corrosion and wear is essential.

Laser surface alloying (LSA) and laser cladding are important technologies, widely used to improve surface properties of Al alloys [2,7–15], titanium alloys [16–19], magnesium alloys [20,21], copper alloys [22], nickel-copper alloys [23,24] and stainless steels [25–27]. However, with LSA process the selection of the alloying elements, compositional ratio and elemental surface distribution is crucial since it has a paramount effect towards microstructural development in the alloyed layer [28]. Due to

high hardness, low density, high melting temperature and good wear and corrosion resistance, ceramics such as carbide, oxide and boride (SiC, TiO_2, WC, TiC and TiB_2) are frequently used as the coating material on Al alloys [2,7–15,29]. During high-intensity laser-matter interaction hard ceramic particles may dissolve and causes the formation of new compounds within Al matrix during solidification. Although, these newly formed compounds may contribute to improved surface integrity, on the other hand, ceramic remnants in the alloyed layer, may retain their original superior properties [4]. Titanium has been often added to react with the carbon in solution forming TiC to improve the surface properties and by the same to prevent the formation of Al_4C_3 carbides [4,8]. TiC is one of the most suitable ceramic materials for the preparation of metal-based ceramic wear-resistant coatings, due to its hardness, stability and exceptional wear resistance [30]. TiB_2 is the most inert, stiffest, hardest of all the borides, characterized by a high melting point, low specific weight, high mechanical strength, good wear resistance and excellent thermal and chemical stability up to 1700 °C [22,31]. Moreover, single phase ceramics—even fully densified—are not wise choices in structural or wear applications because of their variability in mechanical strength and poor fracture toughness [31]. Coatings that consist of two ceramic components such as, TiC and TiB_2, exhibit even better mechanical properties than coatings containing only one ceramic component [32]. Higher TiC content increases the hardness of the resulting two-component TiB_2/TiC ceramic coating, while the higher content of TiB_2 increases the fracture toughness [32]. Moreover, the hardness of the TiB_2/TiC ceramic composite at room temperature is lower than the hardness of a one-component ceramic coating of the same kind. Even so, at the elevated temperature of about 600 °C the hardness value of two-component TiB_2/TiC coating exceeds the hardness value of a one-component coating TiC or TiB_2 [33]. In our previous work [13] a wide energy gap for TiB_2 and TiC near the Fermi level has been confirmed by the density functional theory (DFT) calculations. DFT results indicate covalent bonding which contributed to enhanced corrosion resistance, compared to the pure metallic bonding in the substrate Al sample. Further, a proper combination of ceramics and metals is crucial to obtain sound, high quality alloyed layer [34]. Ceramic phases provide the demanded high strength, hardness and wear resistance, while the addition of alloy material act as the binding phase, hence effectively reducing the residual stress and tendency of cracking [18].

LSA of Al alloys with optimized parameters and different alloying materials has already been confirmed by various authors as advanced, prosperous, cleaner technology for enhancement of wear and corrosion resistance. Nath et al. [7] reported that as-received Al suffered from severe abrasive wear, at the initial stage due to the accumulation of worn out debris at the interface between the mating surfaces. On the other hand, after LSA of WC + Co + NiCr the wear rate was very low and remained constant throughout the test. Mabhali et al. [8] confirmed the highest wear resistance after LSA using a composition of 40 wt.% SiC and Ti and Ni powders ranging from 20 wt.% to 40 wt.%. Rajamure et al. [35] argued that LSA of Mo on Al resulted in the formation of various hard intermetallic phases (Al_5Mo, Al_8Mo_3, Al_4Mo and $AlMo_3$) thereby increasing the coating wear resistance for about 5.5 times compared to the substrate material. In addition, Covino et al. [36] showed significantly higher corrosion resistance of Ti + TiC composite coating in acidic solution compared to the Ti + TiB_2 coatings. Lekatou et al. [37] confirmed corrosion resistant and durable HVOF WC-17Co/Ni-5Al composite coating on Al7075 over a long 49 days exposure in a salt spray chamber. Via cyclic polarization tests Rajamure et al. [3] confirmed substantial corrosion resistance enhancement of LSA Al-W coatings, with reduced corrosion current density and lower anodic dissolution. Shon et al. [38] confirmed homogenous composition and microstructure with enhanced corrosion resistance of HEA (high-entropy alloy) double-layered coatings. Moreover, double-layered coating processed with 21 J/mm^2 experienced minor amount of pitting, whereas with 25 J/mm^2 basically no pitting corrosion occurred due to minimum compositional dilution and uniformity of multi layered HEA phase coating. On the other hand, it was reported [1] that LSA samples with Ni and Ni-Ti-C experienced poorer corrosion resistance of all compared to the untreated alloy A356. Several authors investigated the wear resistance of laser alloyed surfaces on Al alloy with ceramic powders. On the other hand, relatively few studies have investigated corrosion behaviour of LSA powder precursor coatings on Al alloy. Although, laser alloyed TiB_2 and TIC ceramic

powders on Al alloy has already been carried out previously [13–15] a detailed study focusing on effect of different laser energy density (LED) during LSA of TiB_2/TiC/Al composite coatings on HAZ/LMZ, wear and corrosion resistance has not yet been done.

Hence, the objective of this study was to synthesize wear and corrosion resistant TiB_2/TiC/Al coatings on 6082-T651 Al alloy by LSA process using different energy density. The focus of the present study was to characterize the microstructure, tribological and corrosion behaviour of LSA composite coatings and compare it with the untreated material. The presented results can provide a novel way for fabricating excellent wear and corrosion resistant MMC (metal matrix composite) coatings on various Al alloys and promote their commercial applications, especially, in the automotive and processing industry.

2. Materials and Methods

2.1. Sample Preparation and Laser Surface Alloying Process

In this study, commercial Al alloy EN AW-6082-T651 (AlSi1MgMn) with a chemical composition of 0.87 Si, 0.72 Mg, 0.42 Mn, 0.35 Fe, 0.15 minor element (Cu + Cr + Ni + Zn + Ti) and balance Al (all in wt.%) was used as the substrate material. Using the water jet process, flat samples with dimensions 50 mm × 25 mm × 10 mm were cut from a 10 mm thick rolled plate. Prior to laser surface alloying (LSA) the surfaces were wet-ground using deionized water starting with 400- and 600-grit SiC papers followed by degreasing and cleaning in an ultrasonic bath of distilled water and ethanol. Powder mixture of TiB_2 of 99.5% purity (45 µm particle size), TiC of 99.5% purity (2 µm particle size) and Al of 99.5% purity (45 µm particle size) was used as the precursor material. Al powder was added to TiB_2-TiC ceramic precursor mixture to improve adhesion of the ceramic coating to the substrate. The powders with ratio 40 wt.% TiB_2/40 wt.% TiC/20 wt.% Al were mixed with the water based organic binder (LISI W 15853) and reducer (LISI W15833) obtained from Warren Paint and Color Company (Nashville, TN, USA). To achieve uniform mixing, an agitator was used to mix the slurry for about 15 min, which was then spray deposited onto the substrate coupons using an air-pressurized spray gun. The sprayed coupons were dried for 24 h at 25 °C to remove the moisture and a uniform thickness of approximately 150 µm was maintained as the precursor deposit. LSA of spray deposited composite coatings was conducted using a 3 kW, CW mode diode pumped ytterbium fibre laser IPG YSL 3000 (IPG Photonics, Oxford, MA, USA) with a wavelength of 1070 nm and with a focused uniform laser beam of 1.0 mm diameter on the sample surface.

The laser parameters were selected based on prior experience after many trials in order to obtain a good interface bonding and uniform coating without pores and cracks. The coating was applied to the sample surfaces at two different beam power values (800 W and 1200 W) at a constant traverse speed of 60 mm/s and overlapping rate of 50% (Figure 1). Laser power variation corresponded to a laser energy densities (LED) of 13.3 J/mm^2 and 20 J/mm^2, respectively.

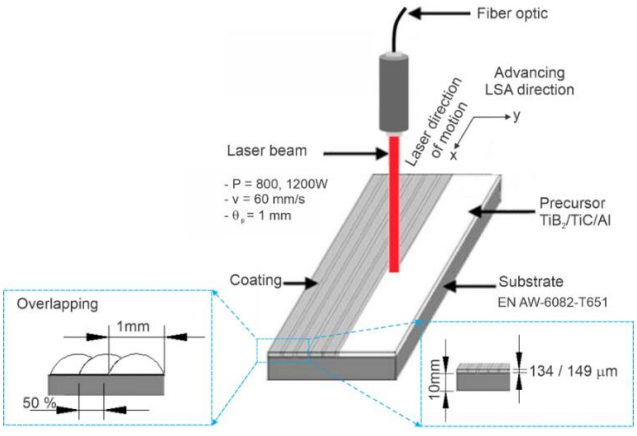

Figure 1. Schematic presentation of laser surface alloying (LSA) experimental procedure.

Since surface condition greatly affect wear and corrosion properties of the materials [13,17] and to directly compare LSA coatings with the untreated material, without the interference from surface roughness, wear and corrosion tests were carried out under the same surface roughness for all samples investigated. Before each wear and corrosion experiment, to match the surface roughness of untreated Al alloy, the LSA samples were wet-ground using deionized water starting with 320-grit paper and continued with 500, 800, 1200, 2000 and 4000-grit SiC papers (Struers ApS, Ballerup Denmark). Between each paper change, the samples were rinsed with deionised water to remove abraded particles.

2.2. Morphological and Microstructural Analysis

Surface morphology and cross-sectional microstructural observation was observed using a Thermo Scientific ESEM FEG Quattro S scanning electron microscope (SEM) (ThermoFisher Scientific, Waltham, MA, USA) equipped with Electron Dispersive Spectroscopy (EDS) microanalysis hardware. EDS point and map analyses in the cross-section were performed with the Ultim® Max SDD detector (Oxford Instruments, Abingdon, UK) at an accelerating voltage of the electrons of 15 kV. Image post-processing, that is, quantitative determination of vol.% of reinforced particles in the LSA layer with was performed using the ImageJ software package (version 1.52t, University of Wisconsin, Madison, WI, USA).

Phase analysis on the LSA samples was conducted using Rigaku III Ultra X-ray diffractometer (XRD) (Rigaku, Tokyo, Japan) with Cu Kα radiation of 0.154 nm wavelength, at 40 kV and 44 mA. Phases were identified in a 2θ range from 20° to 90° with a step size of 0.04° and scan speed of 3° min^{-1}. From the XRD spectra crystalline peaks/phase analysis was performed with background corrections followed by comparison with the standard ICDD (International Centre for Diffraction Data) files in the JADE software database acquired form the joint committee of powder diffraction standards (JCPDS).

The Surtronic 3+ profile meter, Taylor/Hobson Peumo was employed for surface roughness measurements and the data was processed with TalyProfile Lite software (version 3.1.4, Taylor/Hobson, Leicester, England). The Gaussian profile filter was used with a cut-off wavelength value of 0.8 mm to obtain the roughness profile and separate it from the waviness profile. Roughness measurements on each of the sample surfaces were performed in different direction (0°, 90°, +45° and −45°), using a measuring length of l = 12.5 mm. Afterwards, the average surface roughness value was calculated as the mean arithmetic value R_a.

2.3. Microhardness, Residual Stress and Wear Analyses

Through-depth micro-hardness measurements prior to and after LSA were performed in increments of 50 μm to the depth of 900 μm, using a Vickers Hardness (HV) tester (Leitz, Wetzlar, Germany) at a constant 100 g load and 15 s indentation time. Measuring depth was chosen to obtain an insight to the microstructural variation within the coating, interface region, laser melted (LMZ) and heat-affected zone (HAZ) and the substrate material region of LSA coated samples using different LEDs. In average two separate measurements for each data point were performed and an average value and a standard deviation were calculated. Due to differences in the coating thickness the coordinate origin of the depth (x = 0) has been placed at the coating-substrate interface. Further, in the coatings eighteen measurements was conducted at the middle of the coating, in a randomly selected position, at intervals of 500 μm. Afterwards, average microhardness and a standard deviation was calculated.

Surface transverse σ_x and longitudinal σ_y residual stresses (RS) on the LSA coated samples in regard to the processing direction (Figure 1) were estimated from the Al {311} diffraction peak of Cr-Kα X-rays (2.291 Å) located at the angle 2θ = 139° by a iXRD system (Proto Manufacturing, Oldcastle, ON, CN) using a 2.0 mm collimator. For each measurement point the side inclination method with 9 beta angles with 5° oscillation was adopt and the sin2ψ method with a Gaussian profile fitting was applied for the residual stress analysis. The X-ray elastic constant $S_2/2$ used was 19.54×10^{-6} MPa^{-1}.

Tribological wear tests were performed with a TE77 device (Phoenix Tribology Ltd., Newburg, UK) using a reciprocating non-lubricated sliding configuration with an Al_2O_3 ball, at ambient temperature of 23 °C. Test parameters were as follows—5 mm stroke length, oscillating frequency of 2 Hz, normal

load of 30 N and 7200 cycles (t = 30 min). Same parameters were used for both, the LSA processed as well as for substrate material samples, whereas prior to the test execution LSA coated samples were grinded to achieve the same surface roughness as the base material (BM) and cleaned in an ultrasonic bath of acetone. Each experiment was repeated two times and an average value of coefficient of friction (COF) at the end of the test were calculated. Afterwards, measurements of the cross-sectional areas for the calculation of the worn volume (area multiplied by the average length of the footprint) were assessed by a measurement microscope (Nikon, Tokyo, Japan) at four different locations of the groove and averaged.

2.4. Corrosion Analysis

All electrochemical experiments were conducted, on both the untreated Al alloy and LSA coated samples, using a PAR (Princeton Applied Research) Versastat-4 potentiostat/galvanostat/ZRA and controlled by Versa Studio software (version 2.44.4, PAR/Amtek, Oak Ridge, TN, USA). In the present study naturally aerated (T = 23.3 ± 0.4 °C) 0.5 M NaCl aqueous solution, freshly prepared before each experiment, from laboratory grade NaCl (Sigma Aldrich) and deionised water was used as an electrolyte. Immediately prior to each corrosion experiment, samples were cleaned and degreased in an ultrasonic bath of ethanol followed by deionised water for 3 min each. All samples were prepared and cleaned in the same manner, with the utmost caution. Afterwards, the samples were embedded in a PAR Teflon holder, which served as the working electrode with an exposed surface of 1 cm^2 and then immediately transferred to the electrolytic cell. A conventional three-electrode with a volume of 700 mL cell was employed with a saturated calomel electrode (SCE) as the reference electrode, a pair of graphite rods as the counter electrode and the test sample as working electrode. Each experiment was conducted in the same manner and was carried out two times; afterwards the average of the data along with the standard deviation was calculated in order to obtain reproducibility of the results.

Prior to the initiation of cyclic polarization (CP) test, the surface condition of the working electrode was stabilized at open circuit potential (OCP) and $E_{ocp} = f[t]$ measurements were provided during an incubation period of 1 h. Afterwards, the corrosion potential E_{corr}, was determined at the end of the stabilisation process. Followed by OCP, CP scans were initiated towards anodic direction from −200 mV with respect to the OCP at a sweep rate of 0.5 mV/s. The forward scan was then reversed to cathodic direction at the switching potential (E_{sw}), obtained at a predefined threshold current density of 1 mA/cm^2 and progressed towards the initial potential. After completion of CP test, samples were cleaned ultrasonically in alcohol, rinsed gently with deionised water, dried and stored in a desiccator prior to observation of corroded surface under SEM microscope.

Corrosion potential (E_{corr}) and corrosion current density (i_{corr}) were extracted by the Tafel extrapolation method by using a computer least square analysis with the smallest possible error of fit [39–41]. Furthermore, switching potential (E_{sw}) and the potential at which pits repassivate on reverse scan (E_{prot}) were also obtained [42]. Moreover, in order to obtain quantitative information a protective efficiency (P_{EF}) [3,43], was also calculated (P_{EF} (%) = ($i_{corr,BM} - i_{corr,LSA}$)/$i_{corr,BM}$ × 100), based on the corrosion current density of the base material sample ($i_{corr,BM}$) and of LSA composite coating samples produced with different LEDs ($i_{corr,LSA}$), respectively.

3. Results and Discussion

3.1. Surface Morphology and Microstructural Analysis

Figure 2 shows a typical SEM image of LSA coating with hierarchical/multidirectional structures (left image) as a collateral effect of the raster-type laser scan pattern, constant melting and deposition of the recast material in the form of droplets at higher magnification (right image). Surface roughness, after laser processing, depends on the method of laser operation and laser parameters. In general, the application of different LEDs during LSA result in different effects on the melting of the pre-deposited coating and substrate. At lower LED values, the thermal input is lower, hence the remelting of the coated

layer is smaller, rendering the surface more severely. Accordingly, the mean arithmetic roughness of the coated sample produced with 13.3 J/mm^2 and 20 J/mm^2 were 3.7 ± 0.4 µm and 3.3 ± 0.4 µm, respectively. Nonetheless, both samples resulted in similar effects on the melting of the pre-deposited coating and substrate, which is also reflected in similar coating roughness. This is a good indicator of control and effectiveness of the process. Hence, a proper physical quality of the resultant coating that affect mechanical and chemical performance during its application can be anticipated [15].

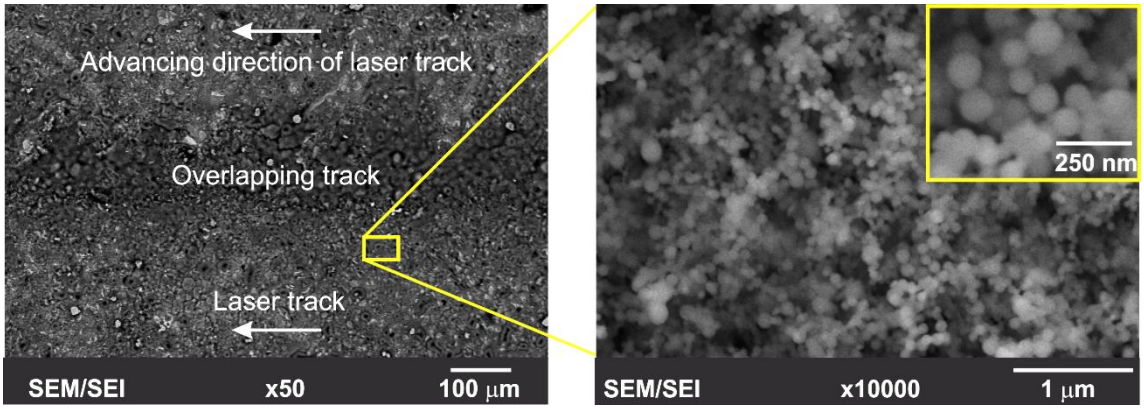

Figure 2. SEM morphology of the LSA TiC/TiB_2/Al coating processed with LED of 13.3 J/mm^2 at lower magnification (left) and at higher magnification (right).

Figures 3 and 4 depicts typical cross-section SEM and EDS map images of the element distribution in cross section of the LSA coated sample after a subsequent surface grinding, respectively. The method of the pre-deposition of the precursor material to the substrate surface resulted in the anticipated coating thickness deviations, which, however, have no significant effect on further results. The average LSA coating thickness produced with 13.3 J/mm^2 and 20J/mm^2, in the as-is condition, were 149 ± 2 µm and 134 ± 3 µm, respectively. Since the coated samples processed with different LEDs showed no significant differences in the microstructure through-depth variation, only one sample, that is, after processing with 20 J/mm^2 was chosen for the presentation. The reinforced particles in the coatings occupy approximately 60–65 vol.% of the total coating volume, being relatively uniformly distributed in the Al matrix but vary in the size (Figure 3a). EDS elemental map of the top coating/interface region in Figure 4a depict that Ti-rich zones consist of TiB_2 and TiC particles whereas the coating matrix is distinguished by the Al rich zone. More importantly, magnesium EDS map revealed alloying effect by the transition of Mg to the coating. As the Mg and Al maps overlap, this indicates the formation of new Al-Mg solid solutions. Mg originated from the substrate Al alloy (AlSi1MgMn) during/after the LSA process since the diffusion coefficient of Mg liquid phase is much greater than for Al-solid phase in the top coating that has rapidly solidified. Hence, the Al/Mg interface also migrated toward the Al-solid phase in the coating [44].

However, the microstructure characteristics of the laser alloyed coatings (e.g., particle size and its distribution) were not influenced by the different LEDs. Moreover, both laser-alloying coatings are free of cracks with low content of porosity and a sound bonding with the continuous and smooth interface between the coating and the substrate. The combination of LSA parameters (power and scanning speed) provided sufficient energy input for the ceramic powder, of low thermal conductivity and the substrate to obtain sufficiently high temperature. Substrate below the coating was efficiently melted, which is of utmost importance to obtain good adhesion between coating and the substrate material.

Measurements of the laser melted zone (LMZ) depth revealed that the thickness of LMZ increases with greater energy input. The depth of LMZ produced with 13.3 J/mm^2 and 20 J/mm^2 were 208 µm and 300 µm, respectively. LMZ at the depth of 100 µm below the interface region (Figure 3b) revealed a remarkably fine distribution of nano-precipitates in the range of 50 nm, consisting of Al, Si, Mg, Mn and Fe (Figure 4b).

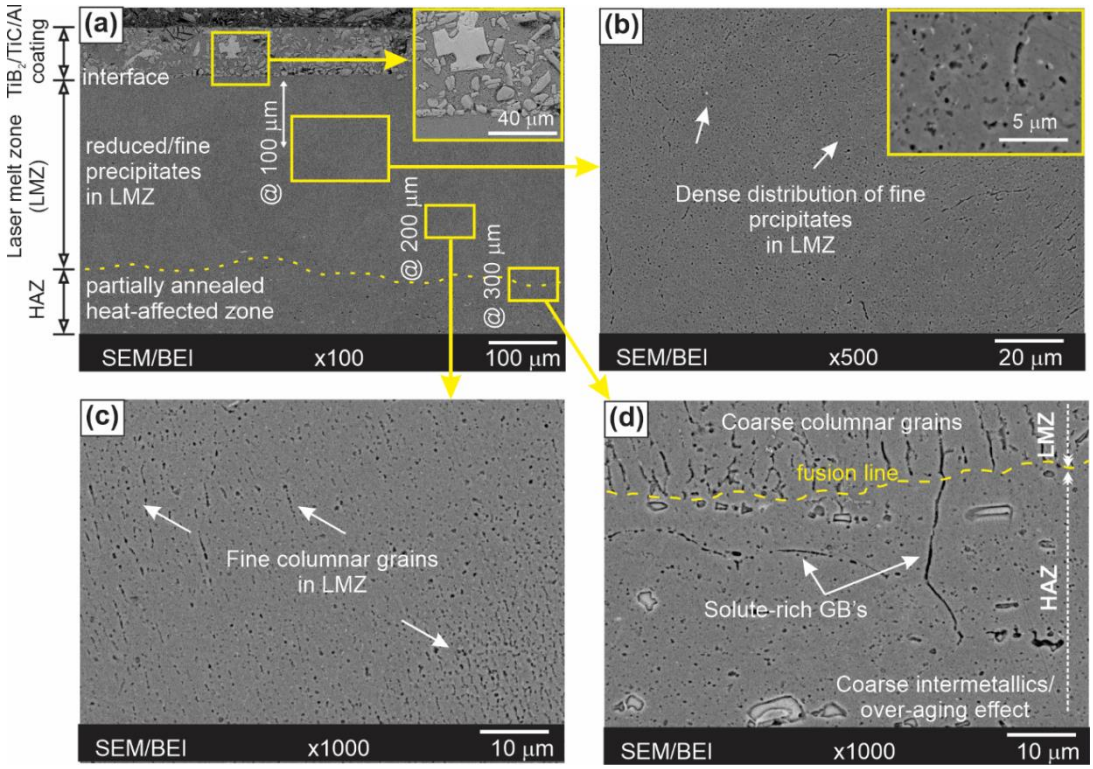

Figure 3. Cross-section SEM/BEI micrographs of the LSA TiC/TiB_2/Al composite coating processed with LED of 20 J/mm^2; (**a**) larger region at lower magnification, (**b**–**d**) magnified images corresponding to the specific region below the interface, marked on (**a**).

These findings indicate that during the LSA process, a temperature was high enough to cause complete melting of the substrate surface below the coating. Due to rapid local solidification, the surface transformed and fine columnar microstructure was formed [12]. Moreover, as evident from Figure 4 high solidification rate during the LSA process caused the alloying elements of the particles to dissolve and mix within the melted layer and then formed fine precipitates [45], which however were still in the "under-aged" condition. The size of the resulting newly formed grains in the LMZ depend on the temperature of the melt during heating and cooling rate. The cooling rates gradually decreased with the depth of the LMZ. Therefore, fine microstructure emerged on the top surface, in the proximity of the interface region, where the cooling rate was the highest, transformed into a coarser microstructure at greater LMZ depths [12].

At the depth of about 200 µm below the interface region (Figure 3c) microstructure exhibit larger columnar grains oriented towards the substrate and the presence of Mg-Si solute-rich grain boundaries (GBs), as can be seen in Figure 4c. Grain coarsening effect is even more evident at the depth of 300 µm (Figure 3d). Here, the largest, coarse columnar grains near the fusion zone are observed, that had grown epitaxially in the direction from the un-melted substrate towards the surface [46]. Beyond this interface, the microstructure was columnar-dendritic which is typical of cast aluminium alloys. Figure 3d depict a distinct boundary between the fusion zone and the substrate material, with unpronounced heat-affected zone, which is typical with laser processing of heat treatable Al alloys [45–48]. Nonetheless, microhardness results (given in the next sections) revealed the HAZ region exceeded a depth of 900 µm, below the interface region, due to the high heat input during LSA process. Excessive heat input has contributed to partially annealing and over-aging effect, contributing to pronounce coarsening of precipitates (Figure 4d) by the coalescence of smaller soluble intermetallic phases [45]. Moreover, in contrast to Figure 3c, where only a few "lonely" GBs were present, a significant feature of segregation and not fully dispersed solute-rich grain boundaries consisting of Mg and Si (Figure 4d) was observed in the proximity of the fusion zone. Both, that is,

continuous and discontinuous GBs bands could be evident (marked in Figure 3d), which may arise from the particles melting, liquation and formation of solute-rich particles along the grain boundary [45,48]. The region with a reduced number of fine, high density precipitates generally represent the weakest zone, hence poorer mechanical and corrosion properties may be anticipated therein.

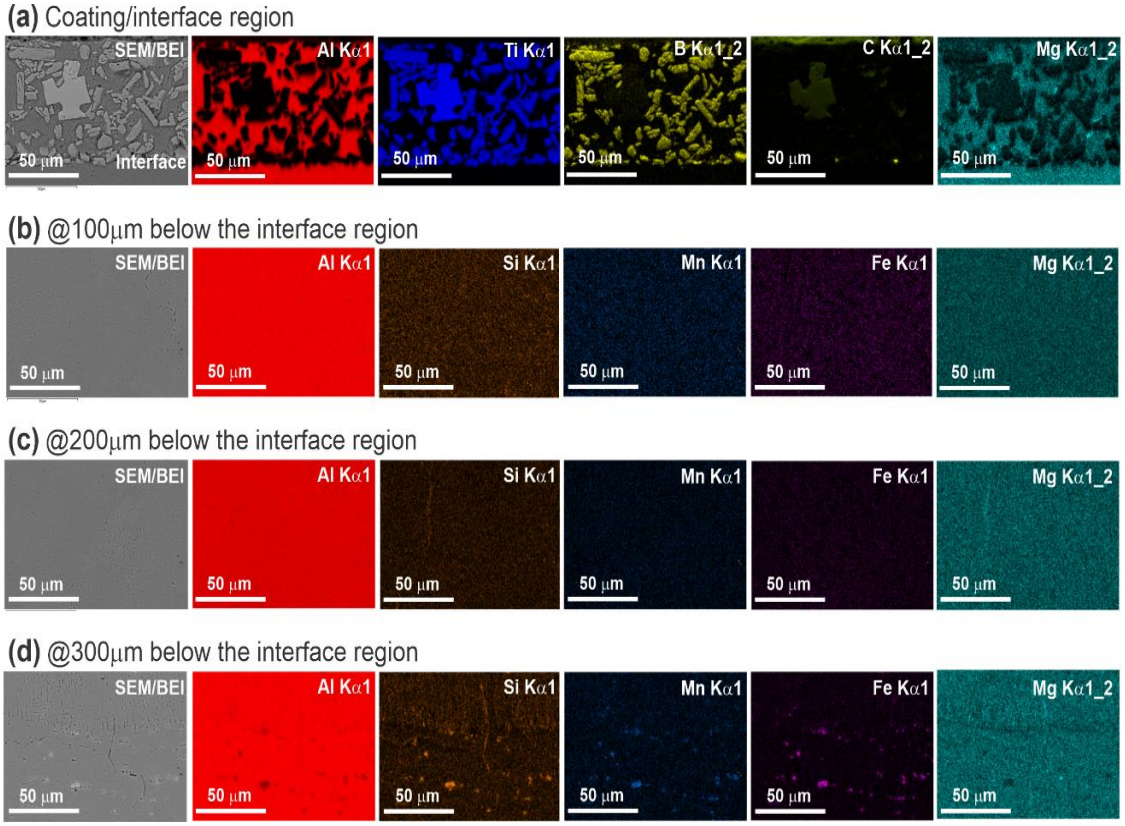

Figure 4. Cross-section EDS elemental distribution maps of the LSA TiC/TiB_2/Al composite coating processed with LED of 20 J/mm^2 corresponding to the specific regions marked on Figure 3; (**a**) at the coating/surface interface, (**b**) 100 μm below the interface, (**c**) 200 μm below the interface and (**d**) 300 μm below the interface region.

XRD analysis of LSA composite coatings on the very top surface revealed the presence of primary TiB_2, TiC, Al phases and secondary B_2O_3, Al_4C_3, Al_2O_3 and TiO_2 phases (Figure 5). A thin passive Al_2O_3 film was formed as a consequence of spontaneous aluminium oxidation on atmosphere [5,49]. Titanium dioxide (TiO_2) is generally formed by the oxidation of the TiC or TiB_2, while B_2O_3 is formed by the oxidation of the TiB_2 [50,51]. Furthermore, it is assumed that after the decomposition of TiC, carbon reacted with aluminium to form aluminium carbide Al_4C_3 [9,52], at the temperature of approximately 940 K [2].

However, one of the major disadvantages associated with LSA process is that it create significant rippling and roughening of the treated surface. This rippling results from two major factors, namely the fluid flow resulting from the shear stresses on the molten film caused by the gradient in surface tension of the liquid film and the vapour pressure above the molten film, which depresses the liquid film [53]. The surface roughness is an important parameter in the tribological contact analysis [17]. During the sliding or rolling of two rough surfaces, the tips of an uneven hard ceramic-coated layer will scratch the opposite surface, resulting in higher friction and wear, especially in the initial sliding phase. Moreover, the surface roughness of the coated layer directly affects the oxidation and corrosion resistance [13]. Flat and smooth surface is likely to be chemically less active in comparison to the rough surface, with a high degree of asperities.

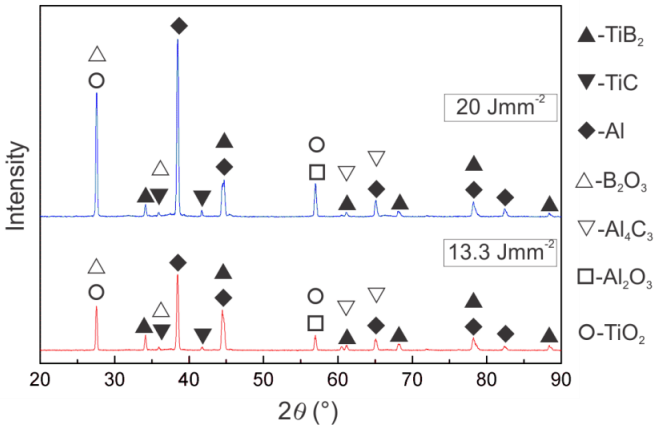

Figure 5. X-ray diffraction (XRD) pattern of the coating produced using different LEDs.

However, wear and corrosion resistant materials are not usually used in the as-treated condition. Therefore, laser alloyed components has to be submitted to some surface finish operation like machining, grinding or even polishing for wear and corrosion applications. Due of this fact, prior to commencement of wear and corrosion experiments, the laser-alloyed coated surfaces were ground using 320–4000 grit SiC papers to achieve an average roughness of 0.8 ± 0.1 μm to match the surface roughness of the untreated Al alloy substrate (i.e., 0.8 ± 0.15 μm).

3.2. Microhardness, Residual Stress and Wear Analyses

Figure 6 illustrates the comparison between top-surface RS and near-surface Vickers micro-hardness (Figure 6a) of LSA samples produced with different LEDs along with the microhardness in-depth profiles of the substrate, Al alloy 6082-T651 and LSA coated samples (Figure 6b). Microhardness measurement confirmed the differences in the microstructure of individual regions, where in the laser-melted zone (LMZ) and the heat-affected zone (HAZ) of LSA coated samples lower values were obtained compared to the untreated Al alloy 6082 in the T651 state (97 ± 4 $HV_{0.1}$) due to heat generation during laser coating processing. Reduced hardness in LMZ was also reported by Katipelli et al. [9] in their research. The relatively low microhardness of LMZ and HAZ was attributed to the dissolution/redistribution of precipitates during LSA process. However, with low laser power the coating and the substrate cannot react adequately, leading to poor metallurgical bonding [4], whereas microhardness of the LMZ and HAZ can easily be improved by the subsequent heat treatment process [14]. Nonetheless, the average microhardness of both LSA coated samples (Figure 6a) were in the range of 164 ± 62 $HV_{0.1}$, which is 69% higher compared to substrate Al alloy. Otherwise, the mean microhardness of sample processed with 13.3 J/mm^2 and 20 J/mm^2 was 148 ± 30 $HV_{0.1}$ and 181 ± 80 $HV_{0.1}$, respectively. Relatively high microhardness deviation is attributed to the different size of reinforced particles and their distribution in the coating.

Randomly selected measurements at the middle of the coating, at intervals of 500 μm, confirm large differences in the microhardness value in dependence of its location (if the measurement was taken on the big and hard reinforcement or if the measurement was conducted in region devoid of reinforcement). Contrary to our results, considerable higher microhardness increase, up to 29 times [7] compared to the original substrate was reported. The main reason for that is the addition of Al to TiB_2-TiC ceramic precursor mixture to improve adhesion, which on the other hand does not significantly improve microhardness. Moreover, Yang and Hu [54] reported that different power densities contribute to the formation of different phases in the alloyed layer, whereas non-equilibrium phases decrease with increasing laser power density. In contrast, Nath et al. [7] argued, that with increased power density the depth of alloyed zone increase as well, however too high power density cause excessive ablation and evaporation of surface elements and micro-cracks can be generated predominantly due to carbide

dissolution. In the present study, no significant variation in the phase constituents as the function of laser energy density was observed.

Afterwards, to investigate the thermal/softening effect due to the heat input produced during LSA process, additional XRD RS measurements were performed on the top surface of the coated samples. Despite high temperature input during LSA process, subsequent melting, recast deposition in the form of molten droplets (Figure 2 (right image)) and relatively large LMZ region (Figure 3), compressive residual stresses (CRS) were measured in both coated samples. For the coating application, CRS are favourable because the surface is able to carry heavier loads and increase the life span. On the contrary, high tensile or shear stresses may result in cracking or the expansion of existing cracks and are therefore undesired. Most likely, CRS originate from the differences in the coefficient of thermal expansion at the coating/substrate interface and/or phase transformations during rapid cooling and solidification. If the coefficient of thermal expansion of the substrate is higher than of the coating and assuming no deformation of the substrate, compressive thermal stresses would have developed in the coating and vice versa [15,55].

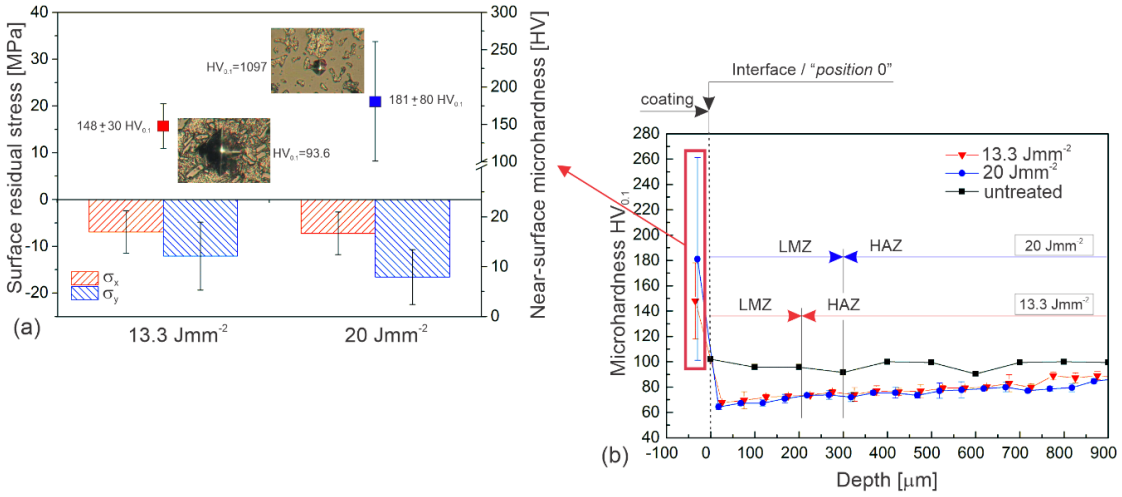

Figure 6. (**a**) Comparison of surface residual stresses and near-surface microhardness in the LSA samples (Inset: HV indentations on the specific region showing the reason for high microhardness deviation) and (**b**) through-depth microhardness profiles.

Sample processed with LED of 20 J/mm^2 achieved a bit higher CRS (σ_y = −16.59 ± 5.88 MPa and σ_x = −7.24 ± 4.57 MPa) compared to the other sample, which was processed with 13.3 J/mm^2 (σ_y = −12.09 ± 7.25 MPa and σ_x = −6.93 ± 4.53 MPa). Results depict smaller CRS values in x-direction of laser motion compared to the advancing, y-direction (see Figure 1). These results are consistent with results reported by other authors dealing with laser treatment on Al alloys [15,43,46].

Often, the greater the hardness, the higher the wear resistance reflecting in lower cumulative mass loss. However, the wear mechanism in case of metal matrix composite is much more complex and can completely differ from classic mechanisms, present in materials with single constituents. Moreover, wear processes strongly depend on microstructural configuration, whereas higher bonding strength between the reinforced particles and soft matrix contributes to lower mass loss [10]. In our case, wear test results confirm the same wear behaviour for both coated samples processed using different LEDs. Wear volume results after the 30 min test presented in Figure 7a clearly depict that both LSA coated samples experienced almost 7-times lower wear volume loss compared to the untreated Al 6082-T651 alloy. The wear volume losses for LSA samples treated with 13.3 J/mm^2 and 20 J/mm^2 are almost the same, that is, (0.34 ± 0.01 and 0.34 ± 0.04) mm^3, while the untreated sample lost 2.34 ± 0.33 mm^3 volume due to wear.

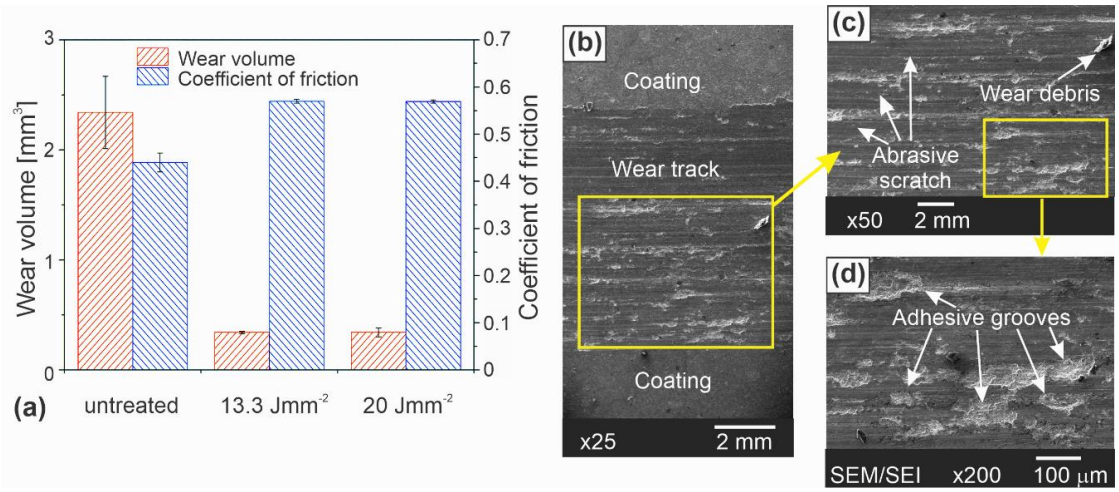

Figure 7. (**a**) Wear volume and coefficient of friction (COF) results of the substrate material and samples processed at different LEDs; (**b**–**d**) SEM/SEI images of wear scars of LSA coated sample processed with 20 J/mm^2.

Metal matrix composites offer considerable enhancement of wear resistance, because the hard ceramic reinforcements impede the removal of material from abrading surfaces [29]. Moreover, it has been shown [7,8], that proper microstructural alteration, bonding, volume fraction, type, shape, size and distribution of the reinforcement particles in metal matrix composites, intermetallic phases and their relationship has to be taken into account when engineering a wear resistant MMC coating. Nath et al. [7] reported significantly lower wear rate of LSA sample due to increased surface hardness. On the other hand, Mabhalli et al. [8] has shown that no direct correlation between hardness and wear resistance exists. Present study revealed no significant variation in the amount and shape of reinforcement as function of laser energy density. In view of this, no differences in the wear behaviour of specific coated samples by different laser coating parameter could be anticipated. Nonetheless, the obtain results clearly indicate that wear resistance of Al alloy can be significantly improved by LSA of TiB_2/TiC/Al composite coatings due to proper interface, crack-free microstructure, higher hardness and induced compressive RS.

Figure 7b shows the worn surface morphology of the LSA sample treated with 20 J/mm^2 after 30 min sliding time. It is evident that the worn surface is relatively smooth with abrasive scratches and some adhesive characteristics. Moreover, wear debris is also observed on the wear surface. In the worn track abrasive wear with many scratches parallel to each other in the sliding direction and adhesive grooves was clearly observed at higher magnification (Figure 7c,d). Delamination by adhesion due to the occurrence of the stick-slip phenomenon is resulting in progressive degradation of the surface [56].

The adhesive wear led to tearing out of relatively large particles of metals from the rubbing surfaces thereby leading to permanent material loss. Moreover, junction formation and interlocking of asperities between the mating surfaces may result also in dislodging of hard TiB_2/TiC particles, which ploughs into the surface and contribute to progressive degradation of the sample surface. Hence, the material loss will depend on how loosely bond the worn-out material is adhered to the surface [25]. However, the wear mechanism of the coatings in this study is mainly comprised of abrasive and adhesive wear. Similar results also reported by other researchers [22,25]. On the other hand, Dai et al. [19] reported that the wear mechanism of the coating is only abrasive wear. However, in the present study Al was added to TiB_2/TiC, resulting in adhesion characteristics on the worn coating surface.

Although, coefficient of friction (COF) provides direct information about the tribology system and the energy to deform the surface of the material, it is not necessarily a direct indication of material loss or separation of loose debris from the surface [9]. COF results after 30 min test presented in Figure 7a indicate non-appreciably effect of LED. Moreover, the average COF obtained with TiB_2/TiC/Al

composite coating was approximately 29% higher compared to the untreated alloy (0.57 ± 0.004 vs. 0.44 ± 0.02). Various authors [22,57] dealing with wear behaviour after LSA treatment reported reduced COF value compared to the original substrate, which is opposite to result from this work. Nevertheless, in their studies different alloying elements and substrates were investigated and this clearly affects the friction behaviour of surfaces in contact. It has been reported that laser alloying with TiN result in considerably lower coefficient of friction [31]. Yean et al. [22] reported significant reduction of COF, using the Ni-Cr-20 wt.%TiB_2-2 wt.%CaF_2 composite coating compared to the copper substrate (0.24 vs. 0.45), especially since CaF_2 is a well-known and widely used solid lubricant. On the other hand, the adhesion strength of the coating/substrate interface has often been a serious problem, which reflected in coating detachment and high COF, that is, in the range of 0.4 to 0.9 [58]. Thus, many researchers reported significantly lower COF values of the substrate material compared to the LSA coated surface performed on aluminium [7] and titanium [17]. Although, results in this study confirmed the beneficial effect of LSA on Al alloy substrate, reflecting in reduced wear, increase of COF would probably be unsuitable for practical sliding component applications like bearings or piston rings vs. cylinder wall contacts [58].

3.3. Corrosion Analysis

3.3.1. Open Circuit Potential

The open circuit potential curves of LSA coated samples and substrate/untreated Al 6082 alloy in a 0.5 M NaCl water solution are displayed in Figure 8. Potential-time transients indicate more negative (active) value of the substrate material sample compared to LSA ones, with lower fluctuations and a gradual potential decrease. In contrast, both laser-alloyed samples demonstrate higher potential values, whereas sample after laser processing with LED of 13.3 J/mm^2 indicate much higher OCP fluctuations compared to the other two samples (10.7 mV vs. 2.8 mV and 2.1 mV). This could be due to the possible dissolution/breakdown/rupture and partial repair/rebuilding effect of the surface layer or it can be an indication of the pitting attack on the laser processed samples [3].

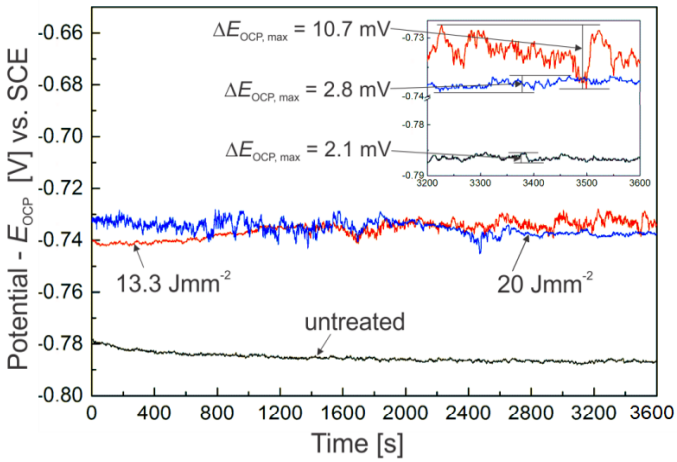

Figure 8. Open circuit potential of different samples in 0.5 M NaCl solution over a period of 1 h.

Nonetheless, all samples achieved steady-state potential after 60 min, indicating an equilibrium state at which the rate of oxidation equals that of reduction, that is, anodic and cathodic reaction at the working electrode/solution interface were balanced [13,43,59]. Further, both laser-alloyed coatings exhibited higher potential Ecorr values at the end of the stabilization process compared to the substrate Al alloy (−734 mV_{SCE} and −738 mV_{SCE} vs. −787 mV_{SCE}). Similar results, that is, small potential differences between laser-alloyed and untreated samples was confirmed in our previous research [13] where different ratios of powder precursor material had been applied for LSA process. Therein, more

stable, corrosion resistant surface was confirmed during immersion in the corrosive environment, despite small Ecorr ennoblement. To investigate if this holds true also for these LSA processed samples and since OCP transients does not reveal the underlying corrosion kinetics and mechanism of corrosion additional cyclic polarization scans were conducted.

3.3.2. Cyclic Polarization

The cyclic polarization (CP) method enable a detailed insight about the material propensity towards localized corrosion phenomenon, for example, pitting corrosion (a qualitative view of pitting corrosion mechanisms and the tendency of a material to undergo surface pitting) when exposed to specific corrosive environment [3,59]. Cyclic polarization curves corresponding to LSA samples produced with 13.3 J/mm^2 and 20 J/mm^2 are shown in Figure 9a,b, respectively. Results of each laser-alloyed coated sample are presented on a separate graph along with the untreated Al alloy substrate for better and distinctive comparison.

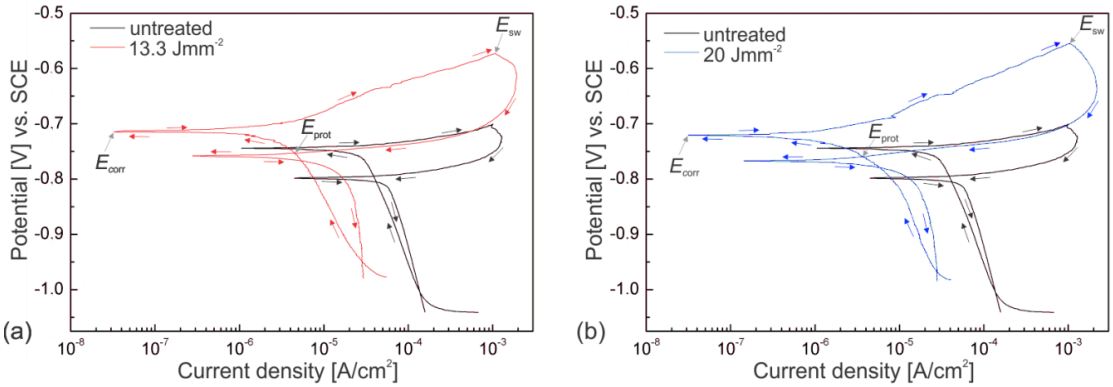

Figure 9. Cyclic polarization (CP) curves in 0.5 M NaCl solution of untreated/substrate and laser processed samples with (**a**) 13.3 J/mm^2 and (**b**) 20 J/mm^2.

Both LSA samples clearly shows similar behaviour, which is expected since the same TiB_2/TiC/Al powder precursor has been used and only different laser energy density (LED) was applied during the manufacturing process. However, in contrast to CP curve of the untreated samples, where a sharp current increase during anodic polarization was present, after LSA process a partial passivation behaviour is observed. Afterwards, increase in anodic current due to a stable pit growth or pit propagation is observed with a well-defined hysteresis in the reverse cathodic region. This fact confirms that both, the untreated Al alloy substrate and laser-alloyed coatings are susceptible to pitting corrosion [60]. Further, although TiC and TiB_2 coating generally exhibit good passivation behaviour in a NaCl solution, the active/Al part of the coatings prevented expressive passive plateau, as the potential continuously increases with increasing current density [1,3,60,61].

Table 1 lists the results of active dissolution potentials obtained from cyclic polarisation tests, including the average values of protective efficiency (P_{EF}). The corrosion potential E_{corr} and corrosion current density i_{corr} were extrapolated using the Tafel extrapolation method. Improvement of all dissolution potential parameters, that is, E_{corr}, E_{sw} and E_{prot}, are obtained after laser alloying due to modification of the passive layer. In general, the more negative the E_{corr}, more actively the surface corrodes. The most positive (noble) E_{corr} potential exhibit the sample processed with 13.3 J/mm^2 (−715 ± 12 mV_{SCE}), while the uncoated Al alloy exhibited the most negative E_{corr} value (−744 ± 17 mV_{SCE}). However, small difference of corrosion potential values and coating variability, a direct conclusion on the relative nobility of the different coatings solely on the basis of E_{corr} cannot be drawn [62]. Further, the most positive protection potential E_{prot} exhibited the sample processed with 13.3 J/mm^2 (−754 ± 7 mV_{SCE}), while the highest switching potential E_{sw} is observed after LSA with 20 J/mm^2 (−555 ± 6 mV_{SCE}).

Table 1. Electrochemical parameters obtained from the CP curves in 0.5 M NaCl solution.

Parameter	Sample Designation		
	Untreated Al Alloy	**Laser Treated/13.3 (J/mm^2)**	**Laser Treated/20 (J/mm^2)**
E_{corr} (mV_{SCE})	−744 ± 17	−715 ± 12	−720 ± 11
E_{sw} (mV_{SCE})	−701 ± 11	−574 ± 8	−555 ± 6
E_{prot} (mV_{SCE})	−795 ± 14	−754 ± 7	−757 ± 13
i_{corr} (μA/cm^2)	29.4 ± 2.86	3.38 ± 0.35	3.12 ± 0.29
P_{EF} (%)	/	88.50	89.39
$E_{sw} - E_{corr}$ (mV)	43 ± 6	141 ± 4	165 ± 5
$E_{corr} - E_{prot}$ (mV)	51 ± 3	39 ± 5	37 ± 2

Moreover, the highest i_{corr} reduction (3.12 ± 0.29 μA/cm^2) was obtained with the sample processed with higher LED (20 J/mm^2), while the untreated Al alloy sample obtained i_{corr} of 29.4 ± 2.86 μA/cm^2. This confirm 9.4 times lower corrosion current density value after LSA treatment. Sample processed with 13.3 J/mm^2 achieved 8.7 times lower i_{corr} value compared (3.38 ± 0.35 μA/cm^2 vs. 29.4 ± 2.86 μA/cm^2). Further, the average protection efficiency results indicate an obvious beneficial effect of the laser alloying process with both laser energy densities, with the highest value of 89%. The substantial enhancement in P_{EF} compared to untreated Al alloy may be attribute to suppression of the cathodic reaction rate due to the microstructure/phases developed during LSA.

All these electrochemical values indicate the worst corrosion resistance of an untreated/substrate sample in a test solution. In addition, the most important ΔE parameter to describe the resistance to the pitting corrosion in chloride containing solution, that is, $E_{sw} - E_{corr}$ and $E_{corr} - E_{prot}$, were examined. The larger value of $E_{sw} - E_{corr}$, indicates a lower degree of anodic dissolution of material, while a smaller value of $E_{corr} - E_{prot}$ presents an improved ability for material repassivation [3,43,63]. Results of ΔE trends in Figure 10 confirm that both laser-alloyed samples provide lower dissolution in the anodic scan and better and faster ability for repassivation in the cathodic scan afterwards the corrosion has occurred.

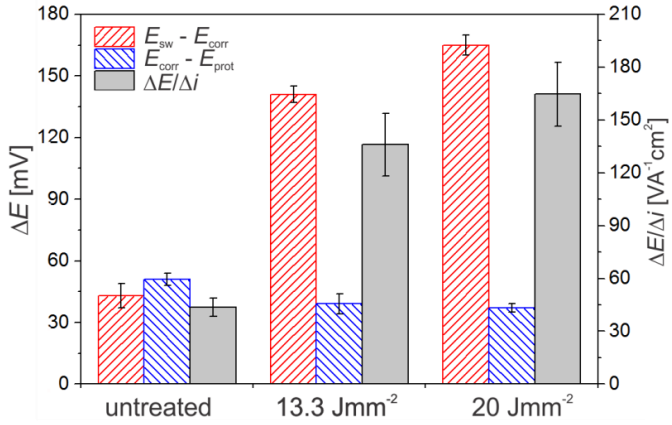

Figure 10. Comparison of ΔE trend as a function of samples in 0.5 M NaCl solution.

Afterwards, to obtain additional insight of general resistance against anodic dissolution in a Cl^- environment, the ΔE/Δi gradient, proposed by Trdan et al. [63,64], was considered. Analysis confirmed a distinctive shift in ΔE/Δi gradient with the LSA samples, with more than 211% higher value compared to the untreated one. For the comparison, untreated sample achieved a value of 43.64 ± 5.24 VA^{-1}cm^2, followed by sample processed with 13.3 J/mm^2 (135.93 ± 17.67 VA^{-1}cm^2), whereas the sample treated with 20 J/mm^2 achieved a maximum value of 164.67 ± 18.11 VA^{-1}cm^2, which is 277% higher ΔE/Δi gradient obtained with the untreated Al alloy sample. These results imply a substantial increase in corrosion resistance of LSA TiC/TiB_2/Al composite coated samples compared to the untreated/substrate

Al alloy sample. Increased resistance to anodic dissolution and reduced pitting propagation rate can be attributed to more chemical stable surface state and to the development of surface CRS [43,65].

Figure 11 shows typical SEM/BEI micrographs of the surface condition after polarization tests of LSA TiC/TiB_2/Al composite coating sample (Figure 11a) and the untreated/substrate Al alloy sample (Figure 11b). Since both laser processed samples revealed similar surface condition after the CP test, only one sample, that is, processed with LED of 13.3 J/mm^2 was chosen for the presentation. SEM examination in Figure 11 indicate pitting attack on both samples, whereas the untreated one shows inferior surface integrity with intense, widespread crystallographic and pitting attack. Further, EDS analysis of the untreated sample confirmed that crystallographic corrosion attack occurred by the extensive matrix dissolution around second phase precipitates (inset on Figure 11b, whitish colour). These cathodic Al(Fe,Si,Mn) precipitates with high Fe/Mn ratio (Fe = 12.62 wt.% and Mn = 6.29 wt.%) are nobler to the Al matrix, which cause higher sensitivity and matrix dissolution in the precipitate proximity [42,63]. In contrast, LSA coated samples after CP tests (Figure 11a) revealed great improvement with lower intensity of corrosion attack. Although, some corrosion attack was detected it was mainly confined to few isolated regions (possible areas of non-homogeneity, proximity of intermetallic particles, etc.).

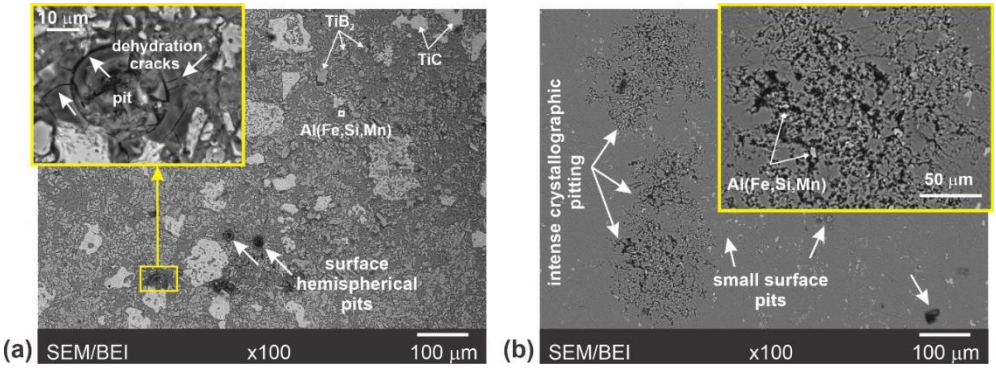

Figure 11. SEM/BEI surface observation after CP measurements in 0.5 M NaCl solution; (**a**) LSA TiC/TiB_2/Al composite coating processed with LED of 13.3 J/mm^2 and (**b**) untreated/substrate Al alloy sample.

However, SEM observations at higher magnification, with the support of EDS analyses revealed, that similar to the untreated Al sample, pitting attack occurred by Al matrix dissolution near nobler intermetallic phases. Such phenomenon is rather logical and expected since Al powder was added to the coating in order to improve the binding and adhesion properties of the interfacial layer but at the same time, increases the corrosion susceptibility. In addition, EDS analysis confirmed almost 2-times lower Cl^- incorporation in the corrosion product on the LSA surface than with the untreated sample. Nonetheless, with all samples, cracks in the corrosion products (inset in Figure 11b) inside the pits were detected due to dehydration after exposure to ambient conditions.

Considering the cyclic polarisation results and SEM observations, it can be concluded that the LSA composite coated samples experienced enhancement in the corrosion resistance in comparison with substrate Al alloy. These are consistent with results reported by Alkhateeb et al. [62], where it was shown that boron content inside Ti-based coatings is highly beneficial in increasing a coating corrosion resistance.

Moreover, TiB_2 dissolution has been shown to result in formation of insoluble hydrated titanium dioxide film which further reduces the corrosion rate. Diao et al. [66] reported that ultrafine structured TiC and TiB_2 improve corrosion performance, having the highest performance with the lowest scan speed of 4 mm/s. Due to the low scanning speed, the composite coating can absorb more power and hence the homogenization of chemical compositions and phases occur.

However, the corrosion resistance of Al and its alloys is not only affected by the bulk microstructure but also the presence of surface defects, which are generated during fabrication process [3]. In the

present study, both coatings were of low porosity and without any cracks. However, the LSA sample processed with higher laser energy density exhibited reduced corrosion current density, lower anodic dissolution and improved ability for material repassivation and reducted pitting attack. Similar results were also reported by Rajamure et al. [3], where higher corrosion resistance was confirmed after LSA using the higher LEDs.

4. Conclusions

TiB_2/TiC/Al coatings with different laser energy density were produced on Al alloy 6082-T651 substrate by LSA process, which effectively improved mechanical, wear and corrosion resistance. Based on the experimental results the following conclusions can be drawn:

(1) The TiB_2/TiC/Al coatings were successfully fabricated with LEDs of 13.3 J/mm^2 and 20 J/mm^2 and were free of defects with sound bonding to the Al substrate.

(2) The average microhardness of the coating is about 69% higher than the untreated material. LSA of Al alloy with TiB_2/TiC/Al does not significantly improve microhardness, due to the addition of Al powder to TiB_2-TiC ceramic precursor mixture to improve adhesion properties.

(3) The coating shows exceptional improvement of wear resistance. After the wear test, the LSA coated samples experienced about eight times lower wear volume loss than the substrate.

(4) From the CP results, it is clearly understood that the untreated/substrate Al alloy shows inferior corrosion resistance compared to the laser processed samples, mainly due to the following facts; (i) substrate Al sample revealed no passive behaviour (while the LSA samples exhibited partial passivation); (ii) untreated Al sample has a much higher corrosion current density (8.7 times higher compared to LSA sample processed at 13.3 J/mm^2 and 9.4 times higher compared to the LSA sample processed at 20 J/mm^2); (iii) higher anodic dissolution (smaller value of $E_{sw} - E_{corr}$) and (iv) more defective surface/higher susceptibility to pitting attack (large value of $E_{corr} - E_{prot}$) compared to the laser processed TiB_2/TiC/Al composite coated samples.

(5) SEM analysis confirmed complete prohibition of crystallographic pitting with LSA samples due to reduced fractional area of liquid-solid interface with chemically more stable surface which prevented the 'chain-link' crystallographic corrosion effect, detected with the untreated/substrate material.

Author Contributions: Conceptualization, D.R, U.T. and R.Š.; data curation, D.R. and U.T.; formal analysis, D.R.; investigation, D.R., U.T. and A.N.; methodology, D.R., U.T. and A.N.; project administration, U.T. and R.Š; resources, R.Š.; supervision, U.T.; writing—original draft, D.R. and U.T.; writing—review & editing, D.R, U.T. and R. Š. All authors have read and agreed to the published version of the manuscript.

Funding: This research received no external funding.

Acknowledgments: The authors acknowledge the financial support from the state budget by the Slovenian Research Agency Programme No. P2-0270. The authors would also like to thank N.B Dahotre and M. Kalin for their assistance with laser surface alloying experiments, XRD phase analysis and wear tests, respectively.

Conflicts of Interest: The authors declare no conflict of interest.

References

1. D'Amato, C.; Betts, J.C.; Buhagiar, J. Laser surface alloying of an A356 aluminium alloy using nickel and Ni-Ti-C: A corrosion study. *Surf. Coat. Technol.* **2014**, *244*, 194–202. [CrossRef]
2. Jiru, W.G.; Sankar, M.R.; Dixit, U.S. Investigation of microstructure and microhardness in laser surface alloyed aluminium with TiO_2 and SiC powders. *Mater. Today Proc.* **2017**, *4*, 717–724. [CrossRef]
3. Rajamure, R.S.; Vora, H.D.; Srinivasan, S.G.; Dahotre, N.B. Laser alloyed Al-W coatings on aluminum for enhanced corrosion resistance. *Appl. Surf. Sci.* **2015**, *328*, 205–214. [CrossRef]
4. Chi, Y.; Gu, G.; Yu, H.; Chen, C. Laser surface alloying on aluminium and its alloys: A Review. *Opt. Laser Eng.* **2018**, *100*, 23–37. [CrossRef]
5. Vargel, C. *Corrosion of Aluminium*; Elsevier: Amsterdam, The Netherlands, 2004.

6. Choudhary, R.K.; Mishra, P.; Kain, V.; Singh, K.; Kumar, S.; Chakravartty, J.K. Scratch behavior of aluminum anodized in oxalic acid: Effect of anodizing potential. *Surf. Coat. Technol.* **2015**, *283*, 135–147. [CrossRef]
7. Nath, S.; Pityana, S.; Majumdar, J.D. Laser surface alloying of aluminium with WC+Co+NiCr for improved wear resistance. *Surf. Coat. Technol.* **2012**, *206*, 3333–3341. [CrossRef]
8. Mabhalli, L.A.B.; Sacks, N.; Pityana, S. Three body abrasion of laser surface alloyed aluminium AA1200. *Wear* **2012**, *209–291*, 1–9. [CrossRef]
9. Katipelli, L.R.; Agarwal, A.; Dahotre, N.B. Laser surface engineered TiC coating on 6061 Al alloy: Microstructure and wear. *Appl. Surf. Sci.* **2000**, *153*, 65–78. [CrossRef]
10. Chong, P.H.; Man, H.C.; Yue, T.M. Laser fabrication of Mo-TiC MMC on AA6061 aluminum alloy surface. *Surf. Coat. Technol.* **2002**, *154*, 268–275. [CrossRef]
11. Katipelli, L.R.; Agarwal, A.; Dahotre, N.B. Interfacial strength of laser surface engineered TiC coating on 6061 Al using four-point bend test. *Mater. Sci. Eng. A* **2000**, *289*, 34–40. [CrossRef]
12. Kadolkar, P.; Dahotre, N.B. Variation of structure with input energy during laser surface engineering of ceramic coatings on aluminum alloys. *Appl. Surf. Sci.* **2002**, *199*, 222–233. [CrossRef]
13. Ravnikar, D.; Rajamure, R.S.; Trdan, U.; Dahotre, N.B.; Grum, J. Electrochemical and DFT studies of laser-alloyed TiB_2/TiC/Al coatings on aluminium alloy. *Corros. Sci.* **2018**, *136*, 18–27. [CrossRef]
14. Ravnikar, D.; Dahotre, N.B.; Grum, J. Microstructure and mechanical properties of TiB_2/TiC/Al coatings on EN AW-6082 substrate produced with laser coating. *Lasers Eng.* **2014**, *29*, 53–68.
15. Ravnikar, D.; Dahotre, N.B.; Grum, J. Laser coating of aluminum alloy EN AW 6082-T651 with TiB_2 and TiC: Microstructure and mechanical properties. *Appl. Surf. Sci.* **2013**, *282*, 914–922. [CrossRef]
16. Song, R.; Li, J.; Shao, J.Z.; Bai, L.L.; Chen, J.L.; Qu, C.C. Microstructural evolution and wear behaviors of laser cladding Ti_2Ni/α(Ti) dual-phase coating reinforced by TiB and TiC. *Appl. Surf. Sci.* **2015**, *355*, 298–309. [CrossRef]
17. Lv, Y.H.; Li, J.; Tao, Y.F.; Hu, L.F. High-temperature wear and oxidation behaviors of TiNi/Ti_2Ni matrix composite coatings with TaC addition prepared on Ti6Al4V by laser cladding. *Appl. Surf. Sci.* **2017**, *402*, 478–494. [CrossRef]
18. Weng, F.; Chen, C.; Yu, H. Research status of laser cladding on titanium and its alloys: A review. *Mater. Des.* **2014**, *58*, 412–425. [CrossRef]
19. Dai, J.; Li, S.; Zhang, H. Microstructure and wear properties of self-lubricating TiB_2-TiC_xN_y ceramic coatings on Ti-6Al-4V alloy fabricated by laser surface alloying. *Surf. Coat. Technol.* **2019**, *369*, 269–279. [CrossRef]
20. Yue, T.M.; Xie, H.; Lin, X.; Yang, H.O.; Meng, G.H. Solidification behaviour in laser cladding of AlCoCrCuFeNi high-entropy alloy on magnesium substrates. *J. Alloy Compd.* **2014**, *587*, 588–593. [CrossRef]
21. Elahi, M.R.; Sohi, M.H.; Safae, A. Liquid phase surface alloying of AZ91D magnesium alloy with Al and Ni powders. *Appl. Surf. Sci.* **2012**, *258*, 5876–5880. [CrossRef]
22. Yan, H.; Zhang, P.L.; Yu, Z.S.; Lu, Q.H.; Yang, S.L.; Li, C.G. Microstructure and tribological properties of laser-clad Ni−Cr/TiB_2 composite coatings on copper with the addition of CaF_2. *Surf. Coat. Technol.* **2012**, *206*, 4046–4053. [CrossRef]
23. Kukliński, M.; Bartkowska, A.; Przestacki, D. Microstructure and selected properties of Monel 400 alloy after laser heat treatment and laser boriding using diode laser. *Int. J. Adv. Manuf. Technol.* **2018**, *98*, 3005–3017. [CrossRef]
24. Kukliński, M.; Bartkowska, A.; Przestacki, D. Laser Alloying Monel 400 with Amorphous Boron to Obtain Hard Coatings. *Materials* **2019**, *12*, 3494. [CrossRef] [PubMed]
25. Lepule, M.L.; Obadele, B.A.; Andrews, A.; Olubambi, P.A. Corrosion and wear behaviour of ZrO_2 modified NiTi coatings on AISI 316 stainless steel. *Surf. Coat. Technol.* **2015**, *261*, 21–27. [CrossRef]
26. Sun, G.F.; Zhang, Y.K.; Zhang, M.K.; Zhou, R.; Wang, K.; Liu, C.S.; Luo, K.Y. Microstructure and corrosion characteristics of 304 stainless steel laser-alloyed with Cr−CrB_2. *Appl. Surf. Sci.* **2014**, *295*, 94–107. [CrossRef]
27. Przestacki, D.; Bartkowska, A.; Kukliński, M.; Kieruj, P. The Effects of Laser Surface Modification on theMicrostructure of 1.4550 Stainless Steel. *KMATEC Web Conf.* **2018**, *237*, 02009.
28. Salim, A.A.; Bidin, N.; Islam, S. Low power CO_2 laser modified iron/nickel alloyed pure aluminum surface: Evaluation of structural and mechanical properties. *Surf. Coat. Technol.* **2017**, *315*, 24–31. [CrossRef]
29. Ramadan, J.M. Abrasive Wear of continuous fibre reinforced Al and Al-alloy metal matrix composites. *JJMIE* **2010**, *4*, 246–255.

30. Wang, X.; Zhang, Z.; Men, Y.; Li, X.; Liang, Y.; Ren, L. Fabrication of nano-TiC functional gradient wear-resistant composite coating on 40Cr gear steel using laser cladding under starved lubrication conditions. *Opt. Laser Technol.* **2020**, *126*, 106136. [CrossRef]
31. Misra, D.; Dhakar, B.; Anusha, E.; Shariff, S.M.; Mukhopadhyay, S.; Chatterjee, S. Evaluation of nanomechanical and tribological properties of laser surface alloyed boride-nitride-carbide ceramic matrix composite coatings. *Ceram. Int.* **2018**, *44*, 17050–17061. [CrossRef]
32. Vallauri, D.; Atias Adrian, I.C.; Chrysanthou, A. TiC-TiB_2 composites: A review of phase relationships, processing and properties. *J. Eur. Ceram. Soc.* **2008**, *28*, 1697–1713. [CrossRef]
33. Telle, R.; Sigl, L.S.; Takagi, K. Boride-Based Hard Materials. In *Handbook of Ceramic Hard Materials*; Riedel, R., Ed.; Wiley-VCH: Weinheim, Germany, 2000.
34. Ahin, Y. Abrasive wear behaviour of SiC/2014 aluminium composite. *Tribol. Int.* **2010**, *43*, 939–943.
35. Rajamure, R.S.; Vora, H.D.; Gupta, N.; Karewar, S.; Srinivasan, S.G.; Dahotre, N.B. Laser surface alloying of molybdenum on aluminum for enhanced wear resistance. *Surf. Coat. Technol.* **2014**, *258*, 337–342. [CrossRef]
36. Covino, B.S., Jr.; Alman, D.E. Corrosion of titanium matrix composites. In Proceedings of the 15th International Corrosion Congress, Granada, Spain, 22–27 September 2002.
37. Lekatoua, A.; Zois, D.; Karantzalis, A.E.; Grimanelis, D. Electrochemical behaviour of cermet coatings with a bond coat on Al7075: Pseudopassivity, localized corrosion and galvanic effect considerations in a saline environment. *Corros. Sci.* **2010**, *52*, 2616–2635. [CrossRef]
38. Shon, Y.; Joshi, S.S.; Katakam, S.; Rajamure, R.S.; Dahotre, N.B. Laser additive synthesis of high entropy alloy coating on aluminum: Corrosion behaviour. *Mater. Lett.* **2015**, *142*, 122–125. [CrossRef]
39. Li, S.; Dong, H.; Shi, L.; Li, P.; Ye, F. Corrosion behavior and mechanical properties of Al-Zn-Mg aluminum alloy weld. *Corros. Sci.* **2017**, *123*, 243–255. [CrossRef]
40. Trdan, U.; Hočevar, M.; Gregorčič, P. Transition from superhydrophilic to superhydrophobic state of laser textured stainless steel surface and its effect on corrosion resistance. *Corros. Sci.* **2017**, *123*, 21–26. [CrossRef]
41. Tiringer, U.; Kovač, J.; Milošev, I. Effects of mechanical and chemical pre-treatments on themorphology and composition of surfaces of aluminium alloys 7075-T6 and 2024-T3. *Corros. Sci.* **2017**, *119*, 46–59. [CrossRef]
42. Trueba, M.; Trasatti, S.P. Study of Al alloy corrosion in neutral NaCl by the pitting scan technique. *Mater. Chem. Phys.* **2010**, *121*, 523–533. [CrossRef]
43. Trdan, U.; Grum, J. Evaluation of corrosion resistance of AA6082-T651 aluminum alloy after laser shock peening by means of cyclic polarisation and ElS methods. *Corros. Sci.* **2012**, *59*, 324–333. [CrossRef]
44. Liu, Y.; Chen, Y.; Yang, C. A study on atomic diffusion behaviours in an Al-Mg compound casting process. *AIP Adv.* **2015**, *5*, 87147. [CrossRef]
45. Nie, F.; Dong, H.; Chen, S.; Li, P.; Wang, L.; Zhao, Z.; Li, X.; Zhang, H. Microstructure and mechanical properties of pulse MIG welded 6061/A356 aluminum alloy dissimilar butt joints. *J. Mater. Sci. Technol.* **2018**, *34*, 551–560. [CrossRef]
46. Watkins, K.G.; Liu, Z.; McMahon, M.; Vilar, R.; Ferreira, M.G.S. Influence of the overlapped area on the corrosion behaviour of laser treated aluminium alloys. *Mater. Sci. Eng. A* **1998**, *252*, 292–300. [CrossRef]
47. Yue, T.M.; Yan, L.J.; Chan, C.P.; Dong, C.F.; Man, H.C.; Pang, G.K.H. Excimer laser surface treatment of aluminum alloy AA7075 to improve corrosion resistance. *Surf. Coat. Technol.* **2004**, *179*, 158–164. [CrossRef]
48. Viejo, F.; Coy, A.E.; García-García, F.J.; Merino, M.C.; Liu, Z.; Skeldon, P.; Thompson, G.E. Enhanced performance of the AA2050-T8 aluminium alloy following excimer laser surface melting and anodising processes. *Thin Solid Film.* **2010**, *518*, 2722–2731. [CrossRef]
49. Vieira, A.C.; Rocha, L.A.; Papageorgiou, N.; Mischler, S. Mechanical and electrochemical deterioration mechanisms in the tribocorrosion of Al alloys in NaCl and in $NaNO_3$ solutions. *Corros. Sci.* **2012**, *54*, 26–35. [CrossRef]
50. McCauley, R.A. *Corrosion of Ceramic and Composite Materials*; M. Dekker: New York, NY, USA, 2004.
51. Cao, G.J.; Xu, H.Y.; Zheng, Z.-Z.; Geng, L.; Masaaki, N. Grain size effect on cyclic oxidation of (TiB_2+TiC)/Ni_3Al composites. *Trans. Nonferrous Met. Soc. China* **2012**, *22*, 1588–1593. [CrossRef]
52. Kennedy, A.R.; Weston, D.P.; Jones, M.I.; Enel, C. Reaction in Al-Ti-C powders and its relation to the formation and stability of TiC in Al at high temperatures. *Scr. Mater.* **2000**, *42*, 1187–1192. [CrossRef]
53. Das, D.K. Surface roughness created by laser surface alloying of aluminium with nickel. *Surf. Coat. Technol.* **1994**, *64*, 11–15. [CrossRef]

54. Yang, Y.; Hu, J.D. Effects of laser power density on the microstructure and microhardness of Ni−Al alloyed layer by pulsed laser irradiation. *Opt. Laser Technol.* **2011**, *43*, 138–142. [CrossRef]
55. Kadolkar, P.B.; Watkins, T.R.; De Hosson, J.T.M.; Kooi, B.J.; Dahotre, N.B. State of residual stress in laser-deposited ceramic composite coatings on aluminum alloys. *Acta Mater.* **2007**, *55*, 1203–1214. [CrossRef]
56. Trdan, U.; Skarba, M.; Porro, J.A.; Ocaña, J.L.; Grum, J. Application of massive laser shock processing for improvement of mechanical and tribological properties. *Surf. Coat. Technol.* **2018**, *324*, 1–11. [CrossRef]
57. Dutta Majumdar, J.; Mordike, B.L.; Manna, I. Friction and wear behavior of Ti following laser surface alloying with Si, Al and Si+Al. *Wear* **2000**, *242*, 18–27. [CrossRef]
58. Holmberg, K.; Matthews, A. *Coatings Tribology, Properties, Mechanisms, Techniques and Applications in Surface Engineering*; Elsevier: Amsterdam, The Netherlands, 2006.
59. Guo, X.W.; Chang, J.W.; He, S.M.; Ding, W.J.; Wang, X. Investigation of corrosion behaviors of Mg-6Gd-3Y-0.4Zr Alloy in NaCl aqueous solutions. *Electrochim. Acta* **2007**, *52*, 2570–2579. [CrossRef]
60. Darabara, M.; Bourithis, L.; Diplas, S.; Papadimitriou, G.D. Corrosion and wear properties of composite coatings reinforced with TiB_2 particles produced by PTA on steel substrate in different atmospheres. *ISRN Corros.* **2012**, *2012*, 898650. [CrossRef]
61. Ferreira, S.C.; Rocha, L.A.; Ariza, E.; Sequeira, P.D.; Watanabe, Y.; Fernandes, J.C.S. Corrosion behaviour of Al/Al_3Ti and Al/Al_3Zr functionally graded materials produced by centrifugal solid-particle method: Influence of the intermetallics volume fraction. *Corros. Sci.* **2011**, *53*, 2058–2065. [CrossRef]
62. Alkhateeb, E.; Ali, R.; Virtanen, S.; Popovska, N. Electrochemical evaluation of the corrosion behavior of steel coated with titanium-based ceramic layers. *Surf. Coat. Technol.* **2011**, *205*, 3006–3011. [CrossRef]
63. Trdan, U.; Grum, J. SEM/EDS characterization of laser shock peening effect on localized corrosion of Al alloy in a near natural chloride environment. *Corros. Sci.* **2014**, *82*, 328–338. [CrossRef]
64. Trdan, U.; Sano, T.; Klobčar, D.; Sano, Y.; Grum, J.; Šturm, R. Improvement of corrosion resistance of AA2024-T3 using femtosecond laser peening without protective and confining medium. *Corros. Sci.* **2018**, *143*, 46–55. [CrossRef]
65. Krawiec, H.; Vignal, V.; Amar, H.; Peyre, P. Influence of the microstructure and laser shock processing (LSP) on the corrosion behaviour of the AA2050-T8 aluminium alloy. *Corros. Sci.* **2011**, *53*, 3215–3221.
66. Diao, Y.; Zhang, K. Microstructure and corrosion resistance of TC2 Ti alloy by laser cladding with Ti/TiC/TiB_2 powders. *Appl. Surf. Sci.* **2015**, *352*, 163–168. [CrossRef]